OPEN ACCESS



From Active Stars to Black Holes: A Discovery Tool for Galactic X-Ray Sources

Antonio C. Rodriguez®

California Institute of Technology, Department of Astronomy 1200 East California Blvd Pasadena, CA 91125, USA; acrodrig@caltech.edu

*Received 2024 January 19; accepted 2024 March 19; published 2024 May 10

Abstract

Galactic X-ray sources are diverse, ranging from active M dwarfs to compact object binaries, and everything in between. The X-ray landscape of today is rich, with point source catalogs such as those from XMM-Newton, Chandra, and Swift, each with $\gtrsim 10^5$ sources and growing. Furthermore, X-ray astronomy is on the verge of being transformed through data releases from the all-sky SRG/eROSITA survey. Many X-ray sources can be associated with an optical counterpart, which in the era of Gaia, can be determined to be Galactic or extragalactic through parallax and proper motion information. Here, I present a simple diagram—the "X-ray Main Sequence," which distinguishes between compact objects and active stars based on their optical color and X-ray-to-optical flux ratio ($F_{\rm X}/F_{\rm opt}$). As a proof of concept, I present optical spectroscopy of six exotic accreting WDs discovered using the X-ray Main Sequence as applied to the XMM-Newton catalog. Looking ahead to surveys of the near future, I additionally present SDSS-V optical spectroscopy of new systems discovered using the X-ray Main Sequence as applied to the SRG/eROSITA eFEDS catalog.

Unified Astronomy Thesaurus concepts: X-ray astronomy (1810); Binary stars (154); Cataclysmic variable stars (203); RS Canum Venaticorum variable stars (1416); Variable stars (1761); Astronomy data visualization (1968); X-ray stars (1823)

Online material: FITS files

1. Introduction

The discovery and characterization of Galactic X-ray sources in the last sixty years opened a new window to the sky and created the field of high energy astrophysics. X-ray observations of M dwarfs, the most common stars in the Milky Way and most common hosts to exoplanets, revealed that these stars are commonly coronally active (e.g., X-rays were detected from 87% of M and K dwarfs within 7 pc of the Sun by Schmitt et al. 1995). X-ray astronomy has also led to the discovery of all of the known accreting neutron star (NS)¹ systems and nearly all stellarmass black hole (BH) systems (Tauris & van den Heuvel 2023), informing our understanding of the most extreme physical environments that cannot be replicated on Earth.

However, it often takes multiwavelength information to decipher the true nature of X-ray sources. Famously, the first stellar-mass BH in the Milky Way, Cygnus X-1, was initially discovered through an X-ray sounding rocket in 1964 (Bowyer et al. 1965). However, it remained uncharacterized for over half a

Original content from this work may be used under the terms of the Creative Commons Attribution 3.0 licence. Any further distribution of this work must maintain attribution to the author(s) and the title of the work, journal citation and DOI.

decade until an optical (and radio) source was associated with the X-ray position in 1971 (Braes & Miley 1971; Murdin & Webster 1971). Precise radial velocity measurements of the optically bright star at the position of Cygnus X-1 were the only way to securely establish that it was a binary companion to a stellar-mass BH (Bolton 1972; Webster & Murdin 1972).

It is with the goal of combining X-ray + optical data to characterize Galactic astrophysical sources that I write this paper. In the days of Cygnus X-1, large error boxes associated with X-ray sources made it difficult to make multiwavelength associations. The pioneering Roentgen satellite X-ray mission (ROSAT; Truemper 1982; Voges et al. 1999; Boller et al. 2016) was the first to image the entire sky with sub-arcminute resolution, and discovered nearly 135,000 X-ray point sources with error circles of radii \lesssim 40" (e.g., Agüeros et al. 2009). However, association with optical sources at that resolution is still difficult, and X-ray + optical association of ROSAT sources in the Galactic plane is nearly impossible (e.g., Salvato et al. 2018).

Today, the landscape of X-ray astronomy is very different. Point source catalogs from X-ray missions that have been active for over 20 yr each contain $\gtrsim 10^5$ point sources and have \sim few arcsecond localizations (θ): XMM-Newton 4XMM-

Radio astronomy has, of course, contributed significantly to our knowledge of NSs as well.

² Though the High Energy Astrophysical Observatory-2 (HEAO-2), also known as the (Einstein Observatory; Giacconi et al. 1979) was the first to image the X-ray sky with 2" resolution, it did not conduct an all-sky survey.

DR13 Catalog (600,000 sources, $\theta \sim 3''$; Webb et al. 2020), Second Chandra Source Catalog (350,000 sources, $\theta \sim 2''$; Evans & Civano 2018), Swift/XRT Point Source Catalog (300,000 sources, $\theta \sim 5''$; Evans et al. 2020). X-ray astronomy is on the verge of being transformed through data releases from the all-sky SRG/eROSITA survey, with millions of X-ray sources localized to a few arcseconds (Predehl et al. 2021; Sunyaev et al. 2021).

The landscape of optical astronomy is also very different, with precise astrometry from Gaia enabling the distinction between Galactic and extragalactic sources (Gaia Collaboration et al. 2016). Large-scale time-domain photometric surveys such as the Zwicky Transient Facility (ZTF; Bellm et al. 2019b), Transiting Exoplanet Survey Satellite (TESS; Ricker et al. 2015), All Sky Automated Survey for Supernovae (ASAS-SN; Kochanek et al. 2017), and Asteroid Terrestrial-impact Last Alert System (ATLAS; Tonry et al. 2018) provide variability information and add a new dimension to optical data sets. Optical astronomy is also on the verge of transformation thanks to the Rubin Observatory Legacy Survey of Space and Time (LSST), which will obtain photometry for nearly an order of magnitude more sources than current time-domain optical surveys (e.g., Ivezić et al. 2019). Just as revolutionary are the multiplexed optical spectroscopic surveys. Millions of spectra are already in the catalog of the Sloan Digital Sky Survey (SDSS; York et al. 2000), and SDSS-V is rapidly increasing that number as well as bringing the advent of multiplex time-domain spectroscopy (Kollmeier et al. 2017). Other surveys include the Dark Energy Spectroscopic Instrument (DESI; DESI Collaboration et al. 2016), the 4 m Multi-Object Spectrograph Telescope (4MOST; de Jong et al. 2019), and the William Herschel Telescope Enhanced Area Velocity Explorer (WEAVE; Dalton et al. 2012).

In this paper, I crossmatch the XMM-Newton 4XMM-DR13 point source catalog and the SRG/eROSITA eFEDS catalog with Gaia to just select Galactic sources. I then present a tool I name the "X-ray Main Sequence," which distinguishes between two main types of Galactic X-ray sources: accreting compact objects (containing a WD, NS, or BH) and active stars. I put forth an empirical cut to separate between the two main types of sources. Finally, I discuss the origin of this clean separation, based on the X-ray saturation properties of solar and late-type stars.

In Section 2, I present cleaned versions of the XMM-Newton and SRG/eROSITA eFEDS catalogs, and the Gaia crossmatch. I also describe each of the Galactic X-ray source classes and the catalogs that I use to provide classifications. In Section 3, I present the X-ray Main Sequence. In Section 4, I present optical spectroscopy of new sources as a proof of concept demonstration, including a crossmatch with early data from SDSS-V. Finally, in Section 5, I provide details on how to make best use of this diagram and why such clean distinction between source classes is possible.

2. Data

2.1. XMM-Newton Source Catalog

I began with the Fourth XMM-Newton Source Catalog, 13th Edition (4XMM-DR13; Webb et al. 2020), which contains 656,997 sources. It is comprised of all publicly available observations taken with the European Photon Imaging Camera in the 0.2–12 keV range between February 13, 2000 and December 31, 2022. Taking overlapping fields into account, this catalog covers \sim 1328 deg² (3%) of the sky. I selected only point sources that do not have any quality flags by making the following cuts:

- 1. Well localized point sources: $SC_EXTENT = 0$ and CONFUSED = 0.
- 2. 5σ detections (with a threshold as described in Webb et al. 2020): SC_DET_ML > 14.
- 3. Low probability of being a spurious detection: SC_SUM_- FLAG $\leqslant 1$.

After these cuts, 368,068 (56% of initial sources) remained. 99% of sources in this final sample have a positional error of (SC_POSERR) <1."95.

2.2. Gaia EDR3 Crossmatch

I then crossmatched the cleaned sources from the XMM-Newton catalog with Gaia Data Release 3 (DR3; Gaia Collaboration et al. 2021, 2023) within a 2" radius.³ I did not account for proper motions since only sources with exceptionally high proper motions (≥100 milliarcsec) would move more than 2" in the maximum ~20 yr difference between XMM-Newton and Gaia observations. Additionally, by using the *stacked* XMM catalog, it is difficult to account for proper motions for sources having been observed potentially years apart. I only kept sources for which there is a single match within 2"−11,161 of the 368,068 clean sources have more than one match, and are predominantly located near the Galactic Center or the centers of clusters, but are excluded here.

I then performed the following cuts on Gaia data to ensure both good quality and that the sources are Galactic:

- Significant parallax and proper motions: parallax_ over_error > 3 and pm/pm_error > 5 in both RA and DEC.
- 2. Significant photometry: phot_mean_flux_over_error >3 in all bands.
- 3. Uncontaminated photometry: phot_bp_rp_excess_ factor_corrected < 0.05.
- 4. Good astrometry: RUWE < 1.4.

This cut left 25,050 sources (3.8% of the original 4XMM-DR13 catalog). I note that I employed rather conservative cuts,

³ The astrometry and photometry in the Early Data Release (EDR3) is identical to that of the newer DR3.

particularly on the parallax. Many Galactic sources could have significant proper motions, while not a parallax. However, the goal of this work is to create a catalog of high confidence Galactic sources.

2.3. Object Classes and Their Catalogs

I used a variety of modern catalogs to provide classifications for known Galactic X-ray objects. As none of these catalogs are by any means complete, ⁴ I instead focused on a high purity fraction for each source classification. I crossmatched all catalogs with the XMM-Newton/Gaia catalog described above to obtain consistent X-ray and optical fluxes. X-ray binaries (XRBs), symbiotics, and spider binaries are exceptions, where the number of sources is low enough that I used X-ray detections from any available detection.

2.3.1. Active Single Stars

Active stars are soft X-ray emitters due to their rapid rotation, which leads to coronal activity (e.g., Pallavicini et al. 1981). Due to their fully convective nature and overall abundance, active M dwarfs are the most common X-ray emitting single stars (Stelzer et al. 2013). I used the sample of 823 active stars from Wright et al. (2011). These systems are located both in the field and in open clusters, and have X-ray detections originally from the ROSAT Bright Source Catalog (Voges et al. 1999). After crossmatching with my XMM-Newton/Gaia catalog, I was left with 112 sources.

2.3.2. Active Binary Stars: RS CVn Systems

RS CVn stars are binaries typically consisting of a slightly evolved subgiant and a solar or late-type star, which may or may not be evolved (Audard et al. 2003). Their orbital periods range from 5–6 hr to tens of days, inducing fast rotation of the stars. This leads to increased activity and X-ray emission (Walter & Bowyer 1981). RS CVns have garnered some attention as being contributors to the Galactic Ridge X-ray Excess (Worrall & Marshall 1983), though the contribution of cataclysmic variables (CVs) is comparable or even higher (Revnivtsev et al. 2006).

There are a handful of well-studied RS CVn systems that receive much attention in the literature (e.g., Sasaki et al. 2021), but I encountered a dearth of large catalogs of vetted systems. Instead, I assembled a list of objects from the International

Variable Star Index (VSX) in the RS category, which yields 73,320 sources. After crossmatching with my XMM-Newton/Gaia data set, this left only 341 systems. Since various well-known RS CVn systems are cataloged as eclipsing binaries (EB*) in the Simbad database, I also included as active binaries systems from my XMM-Newton/Gaia crossmatch that are labeled as EB* and have N > 5 references in Simbad (147 systems). It appears as though the time is right for a dedicated survey of X-ray emitting RS CVn systems.

2.3.3. Young Stellar Objects

Young Stellar Objects (YSOs) are dynamic environments, with the seeds of planets forming in the circumstellar disk extending to hundreds of stellar radii (e.g., Hartmann et al. 2016). The pre-main sequence star at the center is inflated, highly magnetic, and is born rotating rapidly (e.g., Bouvier et al. 1986). This high rotation makes YSOs perfect candidates for being X-ray sources, which were first discovered to be as such by Feigelson & Kriss (1981). However, the high levels of X-ray luminosity, hot (0.5–5 keV) temperatures, variability on hour timescales pointed to a sources of X-rays in addition to coronal activity, such as magnetic reconnection (Feigelson et al. 2002).

I used the catalog of YSO candidates assembled using a crossmatch of Gaia and WISE mid-infrared data (Marton et al. 2019). That catalog was assembled using a training set of well-vetted YSO catalogs to which a Random Forest classifier was used to infer probability of an object being a YSO. I began with all objects in that catalog that have a 96% probability or greater of being a YSO. Of those, 398 are in my XMM-Newton/Gaia crossmatch.

2.3.4. Cataclysmic Variables

CVs are close binaries where a WD accretes from (typically) a late-type main sequence companion (e.g., Warner 1995). In (non-magnetic) CVs where the accretion disk extends down to the WD surface, X-rays originate from the disk-WD boundary layer, while in magnetic CVs where the field is strong enough ($B \gtrsim 1 \, \text{MG}$) to influence the accretion, X-rays originate from the accretion shock on the WD surface (Mukai 2017). CVs are particularly interesting X-ray sources since they are thought to be the dominant contributors to the excess of X-rays from the Galactic Ridge and Galactic Center (Revnivtsev et al. 2006; Hailey et al. 2016).

AM CVn systems are ultracompact CVs ($P_{\rm orb}\approx 5$ –65 minutes), where a WD accretes from a helium-dominated degenerate or semi-degenerate companion. While less than 100 of these systems are known, they are particularly interesting in that some of these will be among the loudest sources of gravitational waves as seen by the Laser Interferometer Space Antenna (e.g., Nelemans et al. 2001; Amaro-Seoane et al. 2017).

⁴ For example, I used the classic Ritter and Kolb catalog of cataclysmic variables (CVs), which contains some of the most well known, spectroscopically verified CVs. This catalog contains 1429 sources, while the larger Open CV Catalog (Jackim et al. 2020), contains over 10,000 sources (mostly candidates).

⁵ Other esoteric classifications also exist: BY Dra stars are K and M dwarfs which show photometric variability on their rotation period (Vogt et al. 1983), and FK Com stars are G and K giants which show similar variability (Bopp & Stencel 1981). Both subtypes are rapid rotators, some of which show evidence for binarity, though the binary fraction of each subtype is unknown.

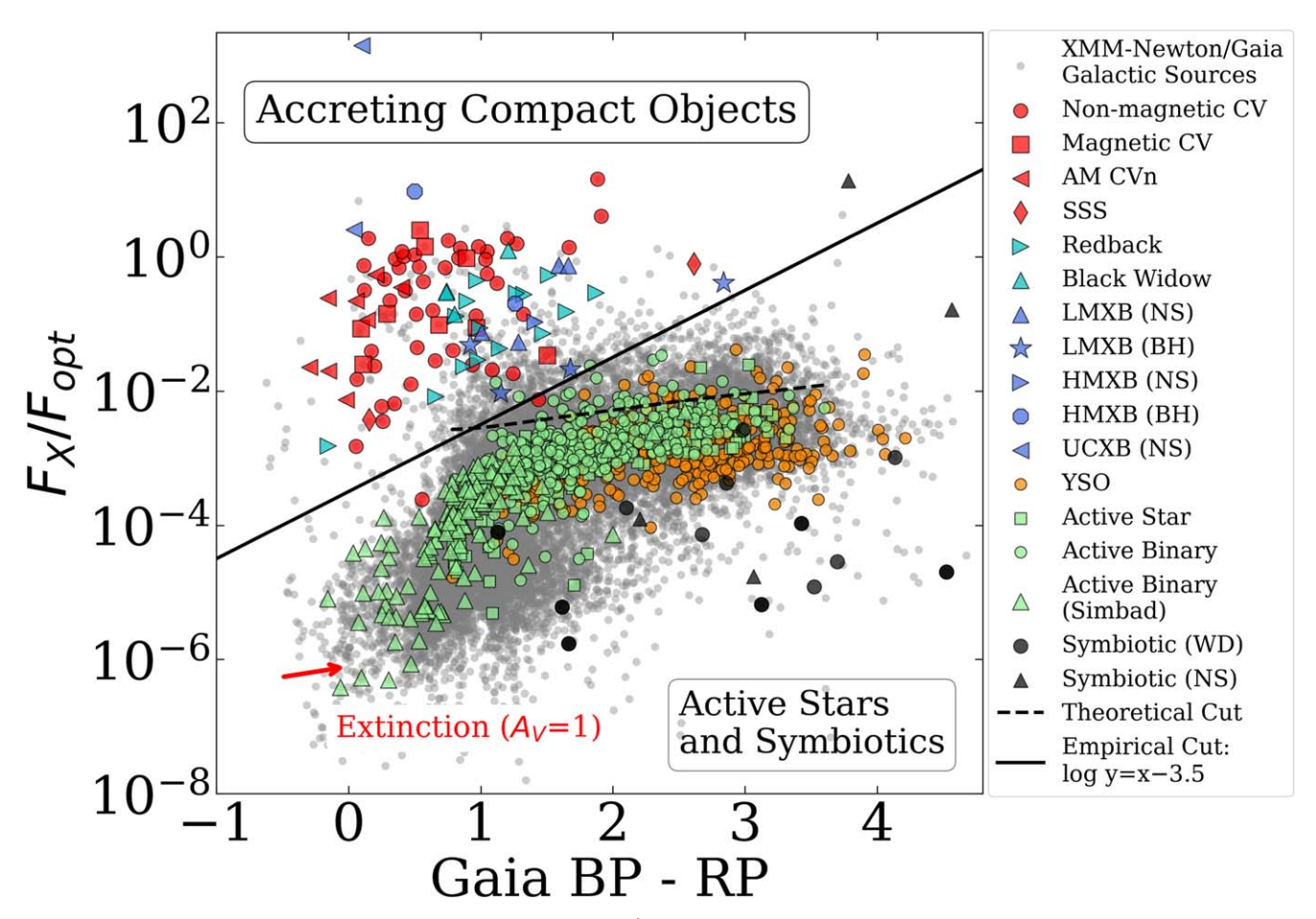


Figure 1. The X-ray Main Sequence. Galactic sources from the XMM-Newton/Gaia crossmatch is shown in gray. Accreting compact object binaries in the upper left are separated from symbiotic and active stars on the bottom right by the "empirical cut" (solid line) or "theoretical cut" (dotted line). All classifications on the right side panel are from the literature, and described in Section 2.3. No extinction correction is applied here, but the extinction vector is shown (de-reddening slides sources toward the lower left).

I used the most updated publicly available catalog of CVs to date, the Final Version (2015 December 31) of the Ritter and Kolb catalog (Ritter & Kolb 2003). This catalog contains 1429 systems primarily discovered through their optical outbursts and/or X-ray associations. 64 of those systems are present in my XMM-Newton/Gaia catalog, including magnetic CVs. Intermediate polars (DQ Her stars) and polars (AM Her stars) are labeled as subtypes DQ and AM, respectively, and AM CVn systems are labeled as type AC.

I also included supersoft X-ray sources (SSSs), which are WDs that have a layer of steadily burning hydrogen on their surface. Their X-ray spectra have equivalent blackbody temperatures ranging from 15–80 eV, which means that little of their bolometric flux overlaps with the XMM-Newton energy range. I used the catalog of SSSs from Kahabka & van den Heuvel (1997) and kept only those systems which have a detection in the XMM-Newton source catalog. 4 systems fulfill

this condition (one is AG Dra, which is a symbiotic SSS and labeled as "symbiotic" in Figure 1).

2.3.5. Millisecond Pulsar (Spider) Binaries

Millisecond pulsars have been found in close binaries with either an M dwarf or brown dwarf companion—redbacks and black widows, respectively. These systems are X-ray sources due to the presence of an intrabinary shock which converts the pulsar power to X-rays (e.g., Romani & Sanchez 2016). While these systems are not accreting, for the purposes of this paper, I will include them in under the umbrella of compact objects, as these systems occupy the upper left portion of the X-ray main sequence. I took the catalog from Koljonen & Linares (2023), which compiles both Gaia positions of known redbacks and black widows as well as their X-ray detections in the literature (all detections come from instruments that would lead to at most a factor of 2–3 correction to the flux in the 0.2–12 keV

range, so I kept original measurements). I omitted all sources labeled as "candidates," and kept only sources that had an X-ray detection, which yielded 15 redbacks and 4 black widows.

2.3.6. Neutron Star and black hole X-Ray Binaries: Low-mass, High-mass, and Ultracompact

XRBs are systems in which a NS or a BH accretes from a binary companion. This takes place in the form of Roche lobe overflow from a degenerate donor star in ultracompact XRBs (UCXBs), Roche lobe overflow from a late-type donor star in low-mass XRBs (LMXBs), and wind accretion from an O/B type star in high-mass XRBs (HMXBs) (e.g., Tauris & van den Heuvel 2023). Most of these systems have been discovered through outburst events, which lead to a transient brightening in both X-rays and optical luminosity (e.g., Lewin et al. 1993). A handful of systems are in a persistent "high" state, accreting near the Eddington limit, and have been visible as bright sources since the early days of X-ray astronomy (e.g., van Paradijs et al. 1988). It is not useful for me to plot LMXBs in outburst, since it defeats the purpose of creating this diagram—to identify persistent Galactic X-ray sources. Instead, I just plotted XRBs which are either in quiescence or in a persistent high state.

I assembled a list of quiescent or high state LMXBs and HMXBs from three papers: Menou et al. (1999) has archival X-ray fluxes of NS and BH binaries before Chandra and XMM-Newton, Garcia et al. (2001) reports results primarily of quiescent BH LMXBs from early Chandra data, and Russell et al. (2006) assembles all known XRB X-ray measurements, distinguishing between quiescent and outbursting sources, NSs and BHs. For the UCXBs, I use the catalog from Armas Padilla et al. (2023), which exclusively has NS accretors.

In all cases, I only kept sources that (1) have a significant Gaia detection and flux measurement (i.e., bright enough and not located in a globular cluster), (2) have detections in a well-defined persistent high state or quiescent state as defined for individual systems in Menou et al. (1999), Garcia et al. (2001), Russell et al. (2006), and (3) have a well-measured X-ray flux (i.e., not an upper limit or marginal detection). This left 2 UCXBs, 4 HMXBs, and 9 LMXBs.

2.3.7. Symbiotic Stars and Symbiotic X-Ray Binaries

Symbiotic stars are long-period ($P_{\rm orb} \gtrsim 200\,$ days) binary systems in which a NS or WD accretes from an evolved, typically a red giant, companion⁶ (e.g., Belloni & Schreiber 2023). The term "symbiotic X-ray binary" is used often in the literature to refer to the subset of systems in which a NS is the accretor. Such systems are prone to X-ray bursts similar to LMXBs and HMXBs.

I used the catalog of WD accretors from Luna et al. (2013) and the catalog NS accretors from Yungelson et al. (2019). To obtain X-ray detections of a few more systems, I crossmatched my XMM-Newton/Gaia catalog with the catalog of symbiotic stars from Akras et al. (2019). I adopted the same quality cuts as in the previous subsection, rendering a total of 11 symbiotic stars with a WD accretor and 4 symbiotic stars with a NS accretor.

2.4. SRG/eROSITA eFEDS Catalog

While data releases from SRG/eROSITA are imminent at the time of writing, the eROSITA Final Equatorial Depth Survey (eFEDS) catalog provides a preliminary look at the final projected sensitivity of the mission. A detailed summary of the survey is outlined in Brunner et al. (2022), and the counterpart association in Salvato et al. (2022). The limiting flux of eFEDS is comparable to that of the XMM-Newton catalog, $F_{\rm X} \sim 6.5 \times 10^{-15} \, {\rm erg \, s^{-1} \, cm^{-2}}$, though with a slightly larger positional uncertainty of 4."7 (Salvato et al. 2022). The full catlagg contains 27,369 sources. In order to select only Galactic sources, I took the catalog of Salvato et al. (2022), and kept only sources with CTP Classification as SECURE GALACTIC or LIKELY GALACTIC. I enforced the same astrometric quality cuts as in the XMM-Newton catalog. Finally, I kept only sources with an X-ray detection likelihood ERO DET ML greater than 10, as suggested by Salvato et al. (2022). This left 1385 sources (5.1% of the original catalog).

2.5. SDSS-V (SDSS DR18) Crossmatch

SDSS recently released its 18th data release (SDSS DR18; Almeida et al. 2023), which includes the first publicly available spectra from SDSS-V (Kollmeier et al. 2017). SDSS-V, among other multiplexed spectrographs (DESI, WEAVE, 4MOST), is undertaking time-domain optical spectroscopic surveys. SDSS-V is uniquely targeting SRG/eROSITA targets, and includes spectra in DR18 of 16,548 objects in the eFEDS patch of sky. This means that even objects without an X-ray counterpart are targeted (Almeida et al. 2023). I crossmatched the SDSS-V eFEDS catalog with the Galactic eFEDS sources described above, and kept only sources with CLASS == STAR and high signal-to-noise SN_MEDIAN_ALL > 10. This left 49 sources, 42 of which pass Gaia quality cuts.

3. The X-Ray Main Sequence

In Figure 1, I present the X-ray Main Sequence, using the XMM-Newton/Gaia crossmatch described above. Most generally, the X-ray Main Sequence can be constructed using any X-ray + optical crossmatch, so long as Galactic objects can be distinguished from extragalactic objects. On the horizontal axis should be an optical color, and on the vertical axis the X-ray to optical flux ratio. To construct this diagram from the XMM-Newton/Gaia crossmatch, I plot the Gaia BP–RP color on the

Symbiotic stars with a BH accretor should in principle exist, but no such systems have been confirmed to date.

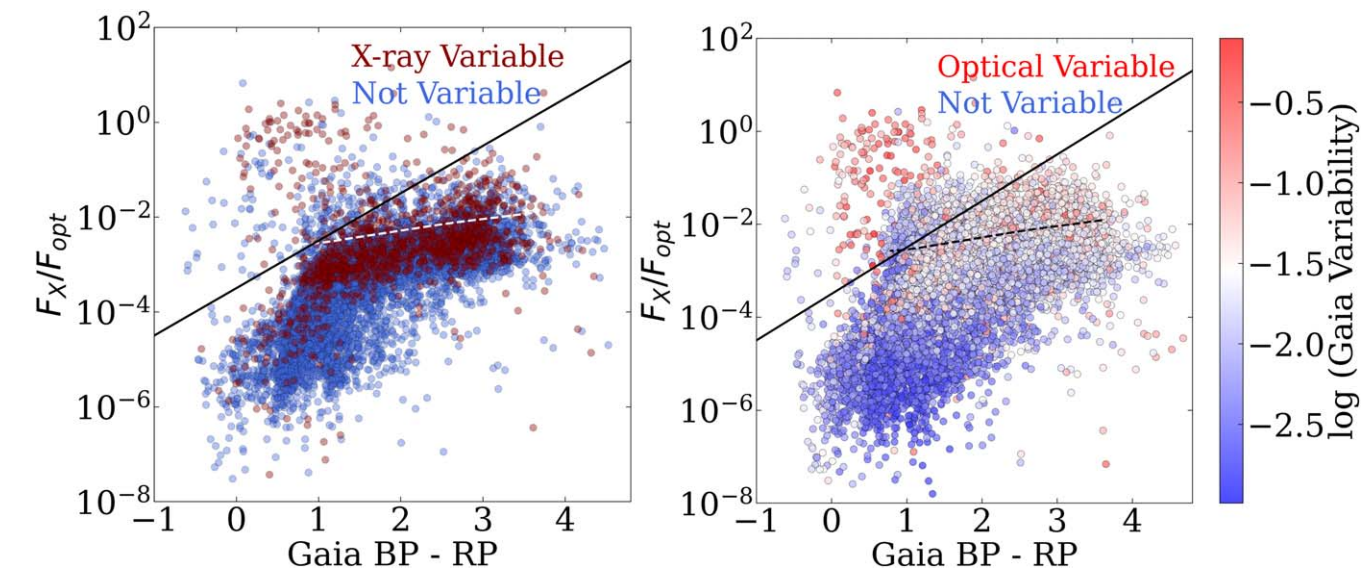


Figure 2. The same data set as in Figure 1, but color coded by X-ray variability (left) and optical variability (right). In both cases, the most variable sources tend to be located above the cut or just below it.

horizontal axis: phot_bp_mean_mag -phot_rp_mean_mag. On the vertical axis, I divide the mean X-ray flux in the 0.2–12 keV band, SC_EP_8_FLUX, by the optical flux in the Gaia G band, $10^{0.4(m_{\odot}-m)}L_{\odot}/(4\pi(1\text{ au})^2)$, where $m_{\odot}=-26.7$ and m is phot_g_mean_mag.

In Figure 1, I show two cuts to distinguish between accreting compact objects and active stars: the "empirical cut" and a "theoretical cut." Symbiotic stars occupy their own region of phase space, below active stars. This means that the diagram can be used to easily separate compact objects with low-mass stellar companions from active stars, but further information is needed to separate out symbiotics (compact objects with evolved donors). The "X-ray Main Sequence" name is attractive since main sequence stars follow their own track, while compact objects occupy separate regions of phase space.⁷

The empirical cut is defined by $\log_{10} y = x - 3.5$, where y is the vertical axis ($F_X/F_{\rm opt}$) and x the horizontal axis (Gaia BP-RP). This cut (drawn by eye) encompasses the majority of accreting compact objects, while removing active stars. More detailed analysis of where to place this cut will be presented in future work. Later in the paper, I discuss the construction of the theoretical cut based on the saturation limit of X-rays stemming from coronal activity of solar and late-type stars.

YSOs and active stars reside below the empirical cut, with YSOs occupying the reddest regions of the diagram and active (binary) stars dominating the bluest regions. Most of the unclassified sources in the diagram have very low $F_{\rm X}/F_{\rm opt}$ values, potentially being active binaries that have not been classified as such.

In Figure 2, I plot the XMM-Newton/Gaia crossmatch, color coded with variability metrics. In the left panel of Figure 2, I color code by the X-ray variability flag, SC_VAR_FLAG (some sources are missing due to the lack of X-ray counts that can be used to compute the variability metric). While non-variable X-ray sources tend to be located everywhere in the diagram, variable X-ray sources are located either in the upper left accreting compact object corner, or in the active star corner, near the boundary.

In the right panel of Figure 2, I color code by an optical variability metric from Gaia. This metric is essentially the mean number of standard deviations from the median flux by which the source varies: $\sigma_G \sqrt{N_{\rm obs}}/\langle G \rangle$ (e.g., Guidry et al. 2021; Mowlavi et al. 2021). The most optically variable sources are, as with X-ray variable sources, either in the upper left part of the diagram or near the boundary between classes. Finally, in Figure 3, I plot all objects with a significant (3 σ) parallax in the 100 pc Gaia Hertzsprung–Russell diagram.

4. Results: Discovery of New Systems as Proof of Concept

In the following subsections, I show the application of this diagram to the discovery of several new objects. This is a pilot study which serves as a proof of concept.

4.1. SRG/eROSITA eFEDS + SDSS-V Optical Spectroscopy

In Figure 4, I present the SRG/eROSITA eFEDS catalog of Galactic objects on the X-ray Main Sequence, along with those objects that have an SDSS-V spectrum in SDSS DR18. As

Though really, this is a color-color diagram.

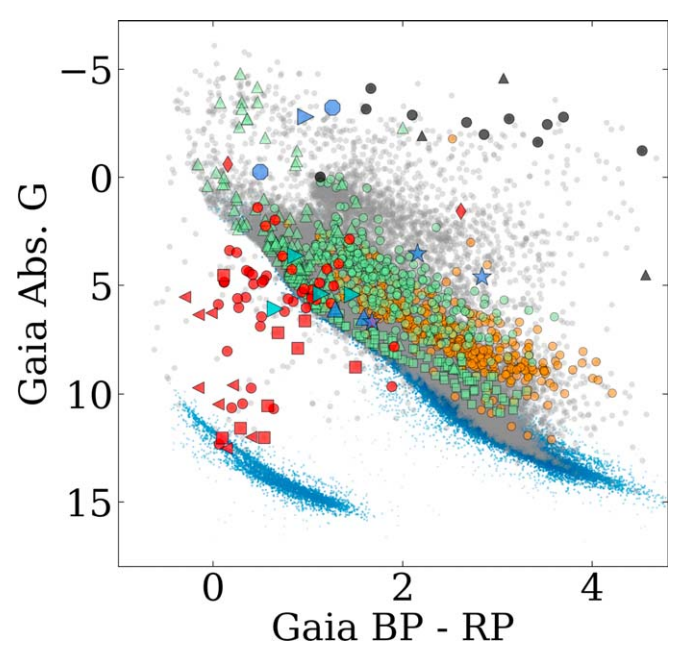


Figure 3. Objects from Figure 1 (same coloring conventions) plotted atop the 100 pc Gaia Hertzsprung–Russell (HR) diagram (light blue). The full XMM-Newton/Gaia crossmatch is shown in gray.

described in Section 2.5, I only keep objects with a high signalto-noise ratio that have CLASS==STAR. I use the same Gaia BP-RP color columns as described in the beginning of Section 3, as well as the same convention when converting from Gaia G to optical flux. However, the SRG/eROSITA band is different than that of XMM-Newton, ranging from 0.2–2.3 keV. I convert the the flux in this band, ML FLUX, to the 0.2–12 keV band, in order to keep all energy bands consistent in both plots. Since the eFEDS field is a small, 140 deg² patch of sky, where the extinction is approximately uniform, I use the WebPIMMS tool8 to convert all fluxes by the same factor. I adopt a power law with $\Gamma = 2$, and A V = 0.093 (Green et al. 2019), which I convert to N H using the relation from Güver & Özel (2009). After this calculation, the values for F_X that I use in Figure 4 are 1.8 times that of ML FLUX.

Using the empirical cut (same as in Figure 1), I classify all objects below the cut as active stars and all above as CVs, though this introduces 4 active stars (10% of objects with spectra) into the CV class. A modified version of the empirical cut, with $\log_{10} y = x - 3$, can be used to cleanly distinguish the two categories. I visually inspect all 42 spectra, and confirm the SUBCLASS classifications in SDSS DR18 (28 M stars, 8 K stars, 1 G star, and 5 CVs). This confirms the effectiveness of the X-ray Main Sequence, though a different empirical cut should ideally be adopted depending on the X-ray telescope, which would have a different energy range. I also note that

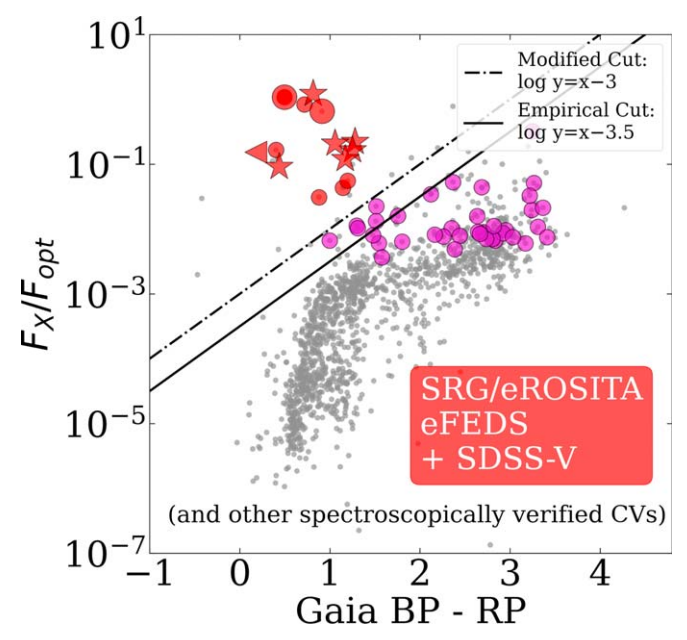


Figure 4. Galactic sources from the SRG/eROSITA eFEDS catalog (gray), with colored circles indicating those that have an SDSS-V spectrum. The two larger circles are polars from Rodriguez et al. (2023b). A "modified" empirical cut, shifted slightly from the one shown in Figure 1, distinguishes CVs (red) from active stars (magenta). Red stars are spectroscopically confirmed CVs from an ongoing survey using the XMM-Newton catalog, and the red triangle is an AM CVn (ultracompact CV) from a separate SRG/eROSITA catalog (Rodriguez et al. 2023a).

targeted objects are predominantly located at high values of $F_{\rm X}/F_{\rm opt}$, likely due to a selection of optically faint objects (e.g., no objects in the eFEDS/SDSS-V crossmatch are brighter than G=16).

The objects in the lower right part of Figure 4 are predominantly active stars, with most M and K dwarfs showing Balmer emission lines or at least $H\alpha$ in emission. However, further work is needed to determine the binary nature of these systems. In Figure 5, I present SDSS-V co-added spectra of four objects (publicly available in DR18) in the eFEDS/SDSS-V crossmatch, one of each spectral type. All four objects are presumably new, with no references in either Simbad or VSX.

4.2. Other SRG/eROSITA Systems: Magnetic CVs and AM CVns

I have shown elsewhere that this diagram can be used to discover two important classes of CVs: magnetic CVs and ultracompact AM CVns. In Rodriguez et al. (2023b), we discovered two polars using a crossmatch of the SRG/eROSITA eFEDS catalog with Gaia and ZTF. In (Rodriguez et al. 2023a), we discovered an eclipsing AM CVn which showed little optical variability due to poor photometric

⁸ https://heasarc.gsfc.nasa.gov/cgi-bin/Tools/w3pimms/w3pimms.pl

⁹ At the time of writing, work is being undertaken to identify all CVs in the eFEDS field (Schwope et al. 2024).

coverage. We demonstrated that it was the X-ray + optical crossmatch and its placement in the X-ray Main Sequence that enabled the discovery and characterization of that object. I show all three systems in Figure 4, with the two polars shown as larger red circles and the AM CVn as a triangle.

4.3. XMM-Newton CVs with Keck and Palomar Spectroscopy

To further demonstrate the effectiveness of the X-ray Main Sequence in selecting accreting compact objects, I am undertaking a spectroscopic survey of CV candidates selected from the upper left corner of the XMM-Newton/Gaia crossmatch presented in this paper (as well as other X-ray catalogs). To complement this survey, I am also crossmatching with optical photometry from the (ZTF; see Appendix A for details). Here, I present six systems from this ongoing survey to highlight the effectiveness of the X-ray Main Sequence. In particular, the systems I present are "exotic CVs"—CVs which have been particularly rare in purely optical surveys (i.e., those that search for optical outbursts). A description of all objects and observations is in Appendix A. Optical spectra of all objects are shown in Appendix Figure 9, and optical light curves in Appendix Figures 10 and 11.

5. Discussion

5.1. How to Interpret This Diagram and Estimates of Purity and Completeness

As discussed in Section 2, the catalogs for all objects types in this sample are almost certainly incomplete. In no way do I claim that this plot perfectly distinguishes between classes of objects. In addition, the majority of objects in the XMM-Newton source catalog, even those with optical counterparts, remain unidentified. So, it is difficult to obtain estimates of either purity or completeness without more detailed classification (e.g., from optical spectroscopy). The most that we can say at the present time is that the empirical cut in Figure 1 introduces at most a few active stars into the accreting compact object corner, and vice versa. However, there are a few CVs and HMXBs that make their way into the bottom right corner, presumably due to high optical contribution from the donor and/or accretion disk. Despite these caveats, the diagram works very well for classifying objects actually detected by X-ray surveys. That's the point: not to find every compact object, but to classify the ones that are X-ray sources.

Nevertheless, estimates of purity and completeness are still possible. Using the literature-classified objects presented in Figure 1, 93 of 98 accreting compact objects (CVs, spider binaries and XRBs, but not symbiotics) are in the upper left corner of the diagram, while 995 of 998 active stars (single stars, binaries, and YSOs) are in the lower right. This leads to the classification of accreting compact objects being 94.9%

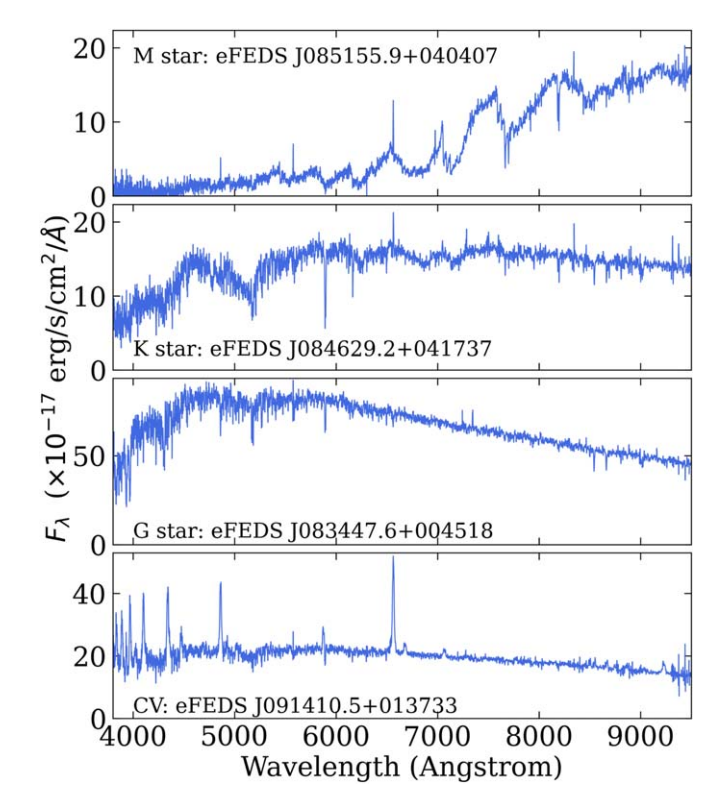


Figure 5. SDSS-V spectra of four objects with distinct spectral types in the SRG/eROSITA eFEDS catalog. All objects are new discoveries, with spectroscopy confirming the predicted classification from the X-ray Main Sequence.

complete and 96.9% pure, while the classification of active stars is 99.7% complete and 99.5% pure. Perhaps most powerful, however, is the efficiency of this diagram in classifying accreting compact objects—of the literature-classified sources, 93 of the 1000 sources (9.3%) are located in the upper left corner, while 562 of the 25,050 sources in the full XMM-Newton/Gaia crossmatch (2.2%) are located in the upper left corner. I elaborate on the importance of this and the application to upcoming targeted surveys in Section 5.4.

5.2. Why This Diagram Works: The Saturation Line

A plausible explanation for the clear clustering in this diagram rests on a well-known empirical result in the study of solar and late-type active stars: the X-ray luminosity "saturates" at the (typically claimed) limit of $L_{\rm X}/L_{\rm bol}\approx 10^{-3}$.

This existence of this X-ray saturation limit has been proposed to be due to the limit on the magnetic field strength as a result of the dynamo mechanism (Reiners et al. 2022). In the earliest works investigating stellar activity, Skumanich (1972) connected the strength of the Ca II H and K lines with stellar rotation periods. Pallavicini et al. (1981) was the first to use X-ray fluxes (from the Einstein Observatory) as a stellar activity indicator and show a dependence of X-ray luminosity

on stellar rotation periods. Later works then used larger X-ray data sets (such as ROSAT) to show that at the fastest rotation periods, X-rays saturate at $L_{\rm X}/L_{\rm bol}\approx 10^{-3}$ (e.g., Reiners et al. 2014; Magaudda et al. 2020; Johnstone et al. 2021). In most cases, $L_{\rm X}/L_{\rm bol}$ is plotted versus the Rossby number, Ro, which is the ratio of the rotation period over the convective turnover timescale. There is also a "super-saturated" regime at the lowest Rossby numbers where $L_{\rm X}/L_{\rm bol}$ turns over and decreases from the saturation limit (e.g., Núñez et al. 2023).

In recent years, it has been proposed that stellar activity and magnetism arise from a dynamo mechanism—where it can be most simply stated that kinetic rotational energy is converted to magnetic energy (e.g., Charbonneau 2014). If the dynamo theory holds, then limits on stellar rotation naturally set a limit on magnetic activity, and therefore X-ray luminosity (Reiners et al. 2022). In Figure 6, I present the sample of 823 active stars from Wright et al. (2011). That data set is comprised of previously known active stars in the field and open clusters, with X-ray detections from the ROSAT Bright Source Catalog Voges et al. (1999). I take the values of L_X , L_{bol} , T_{eff} , and P_{rot} directly from Wright et al. (2011), where details on their calculation of those quantities from various raw data sets are presented. In practice, the saturation limit has a variance of ≈ 0.5 dex, so I adopt a saturation limit of $L_{\rm X}/L_{\rm bol} = 10^{-2.5}$ when creating the "theoretical cut" in the X-ray Main Sequence.

Now that a limit of $L_{\rm X}/L_{\rm bol}$ is established, I convert $L_{\rm bol}$ to a more useful observational quantity: an optical color and luminosity in a single optical bandpass, $L_{\rm opt}$. To compute $L_{\rm bol}$, I take a 10 Gyr isochrone from the MESA Isochrones and Stellar Tracks library (MIST; Choi et al. 2016), at solar metallicity and with $v/v_{\rm crit}=0.4$. The final step is to obtain an optical luminosity, which can be taken at a single optical passband (i.e., Gaia G). I do this by using the Sun's absolute G magnitude as a reference, and computing $L_{\rm opt}=10^{0.4(M_{G,\odot}-M_G)}L_{\odot}$. The steps in creating the theoretical cut are visually outlined in Figure 7.

5.3. Earlier Versions of This Diagram and Previous Classification Efforts

One of the earliest versions of this diagram appears in Figure 1 of Maccacaro et al. (1988), though it is presented as a way to distinguish extragalactic objects from galactic objects using data from the Einstein Observatory. Stocke et al. (1991) later presents this diagram showing only stellar sources, also using Einstein data, but only a few dozen points appear in the plot. Nearly 25 yr later, the diagram re-appeared in Figure 2 of Greiner & Richter (2015) using ROSAT data, now with a clear distinction between AGN and CVs in the upper left and stars in the lower right. However, just a few dozen sources are plotted, and only a limited explanation given as to why the diagram distinguishes between classes. Discouragingly, there appeared

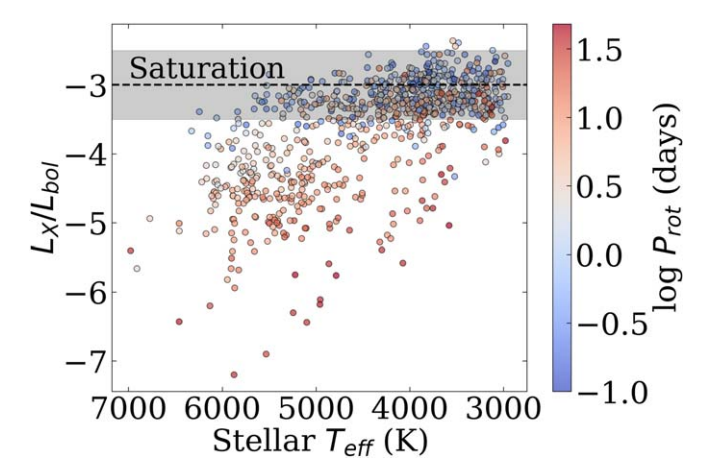


Figure 6. All active stars in the sample of Wright et al. (2011) are below the saturation limit of $L_{\rm X}/L_{\rm bol}=10^{-2.5}$. The majority of stars in the saturated regime tend to be cooler, with $T_{\rm eff} \lesssim 5000$ K.

to be no way to distinguish between AGN and CVs, since they both occupied the same region of phase space (Gaia DR1 would come one year later).

Recently, this diagram has appeared more often in the literature thanks to reanalyzed ROSAT and early SRG/ eROSITA data, Freund et al. (2022) created this diagram for a catalog of stellar sources in ROSAT data, and present a very thorough explanation for the dearth of sources above $F_{\rm X}/F_{\rm opt} = 10^{-3}$ (they also invoke the well-known "saturation limit"). However, compact objects are entirely left out. This diagram is also shown in Appendix B of Stelzer et al. (2022), where optical/X-ray counterparts from the eFEDS survey of the SRG/eROSITA telescope are shown. In that figure, extragalactic and Galactic objects are distinguished, but no further information is presented. Most recently, Schwope et al. (2022) and Schwope et al. (2023) presented studies of two newly discovered CVs and show their location to be in the upper left corner of this diagram alongside other SRG/ eROSITA sources.

I propose three main reasons for the lack of investigation and use of the diagram beyond the studies listed above: (1) there have been fewer X-ray sources in previous surveys compared to today, (2) many of those sources did not even have reliable optical counterparts due to large X-ray error circles, and (3) distinguishing between Galactic and extragalactic sources was much more difficult before Gaia. Many of the large catalogs on which I rely to provide classifications have also only come about in the last decade or so.

Finally, I summarize previous works which have come up with more complex classification schemes of Galactic and extragalactic X-ray sources. Lin et al. (2012) presented a decision tree classifier for 4000 sources in an earlier XMM-Newton catalog, where they classified sources into active stars, active galactic nuclei, and compact objects based on variability

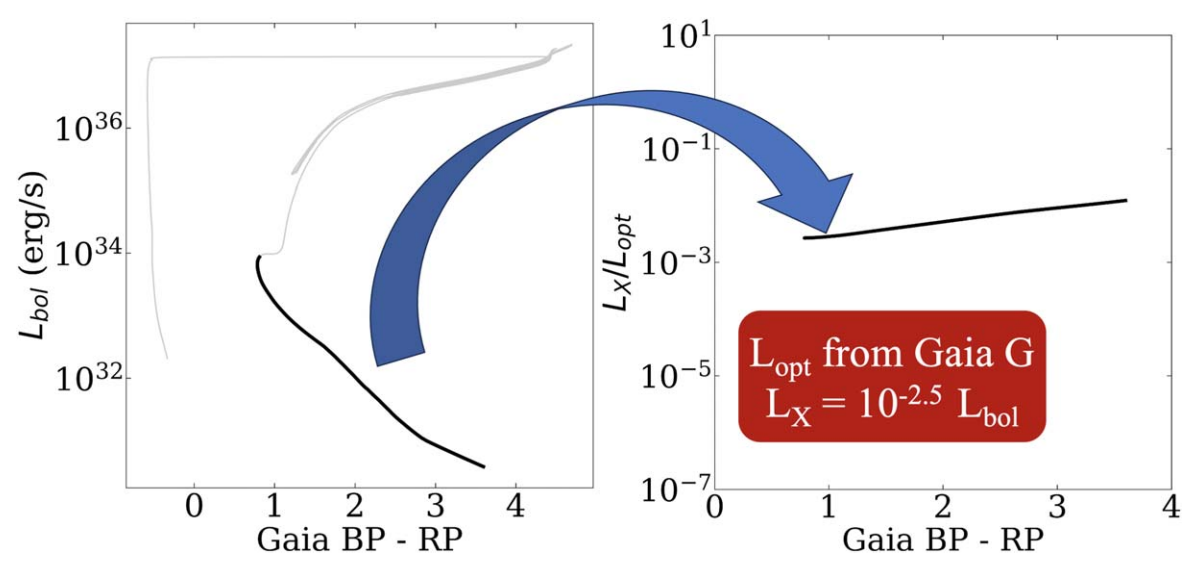


Figure 7. A MIST isochrone at the current age of the Milky Way converts between L_{bol} , an optical color, and L_X . The main sequence is shown in bold, and we omit the evolved tracks shown in lighter color.

metrics and flux and hardness ratios. Lo et al. (2014) built a Random Forest classifier for sources in the XMM-Newton archive, with the goal of classifying sources based on their X-ray variability. However, this work requires high signal-tonoise and long duration observations of the same source (which is very different from the all-sky SRG/eROSITA survey), so that work, though very effective, was limited to study a mere 873 sources. Most recently, the work of Tranin et al. (2022) constructed a Naive Bayes classifier to classify 25,000 known sources in the Swift and XMM-Newton catalogs, which additionally made use of Gaia proper motions. However, they had particular difficulty in recovering CVs, recovering only 34% of known systems, though they are able to recover extragalactic objects and known XRBs more reliably. In a sense, the X-ray Main Sequence serves as a much simpler, and in most cases, more effective discovery tool, in particular for Galactic sources.

5.4. Applications to Upcoming Large X-Ray and Optical Surveys

Given an X-ray detection and identification of an optical counterpart, this tool can efficiently select accreting compact objects candidates for optical spectroscopic follow-up. The efficiency is impressive: of the 25,050 sources in the XMM-Newton/Gaia crossmatch, only 562 (2.2%) of sources are above the empirical cut. Furthermore, because the vertical axis is written as $F_{\rm X}/F_{\rm opt}$, distant or faint objects that may only have a Gaia proper motion (and not parallax) can still be selected.

The most obvious application in the immediate future is for large scale spectroscopic surveys (e.g., SDSS-V, DESI, WEAVE, 4MOST). While these surveys are making obtaining

optical spectra easier than ever, targeting is still needed to be done based on some prior information. I propose that these spectroscopic surveys inform their targeting strategies based on Figure 1. I present a cartoon outlining the main classes in Figure 8.

6. Conclusion

I have presented a tool for X-ray + optical astronomy that has received little to no attention in the past. The power of this tool is effectively demonstrated thanks to modern data sets—in particular, 2" error circles from the large XMM-Newton source catalog, precise astrometry from Gaia, and a whole host of catalogs with object classifications in the literature. The "X-ray Main Sequence" distinguishes accreting compact objects in the upper left from active stars and in the lower right. Symbiotic stars appear to occupy a unique portion of phase space as well.

I have presented two cuts to distinguish between accreting compact objects and active stars: an empirical cut and theoretical cut. The empiricat cut is defined by $\log_{10} y = x - 3.5$, where y is the vertical axis $(F_{\rm X}/F_{\rm opt})$ and x the horizontal axis (Gaia BP–RP). The theoretical cut is based on a well-known relation in active stars, namely that they have a "saturation limit" of $L_{\rm X}/L_{\rm bol} \lesssim 10^{-2.5}$ (though $L_{\rm X}/L_{\rm bol} \lesssim 10^{-3}$ is often quoted in the literature). The cuts I present are not perfect by any means, and could be affected by incompleteness in object catalogs that I use.

In brief, the "X-ray Main Sequence" shows promise for being used as an initial classification tool for upcoming surveys. It is highly efficient at selecting accreting compact objects, flagging a mere $\sim\!2\%$ of objects as candidates. Both X-ray and optical astronomy are on the verge of

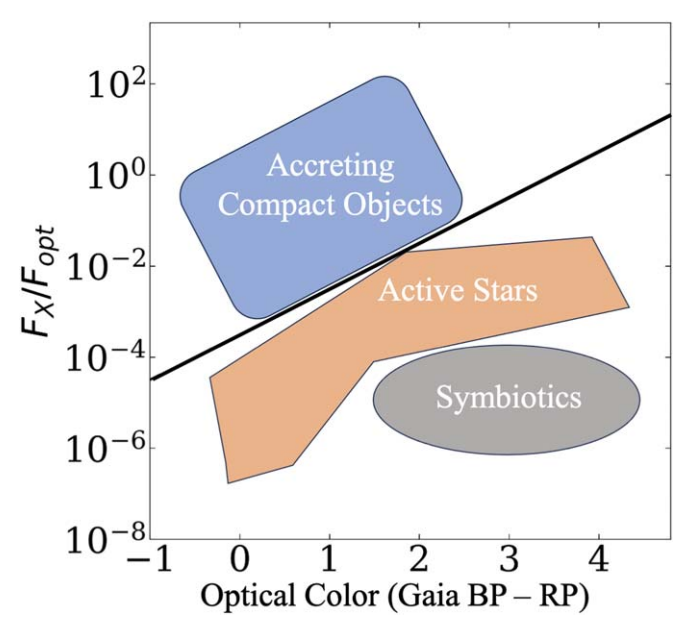


Figure 8. A cartoon of Figure 1 demonstrating the location of the three main categories of objects in the X-ray Main Sequence.

transformation, thanks to SRG/eROSITA, Gaia, the Rubin Observatory LSST, and the growing optical data sets from ZTF, TESS, ATLAS, and ASAS-SN. Stellar astronomy is entering a new golden era, and tools such as this will be crucial in identifying interesting single objects as well as large systematic surveys.

Acknowledgments

I wish to thank Shri Kulkarni and Kareem El-Badry for their thorough reading of this manuscript and useful feedback. I acknowledge useful input from an anonymous referee which led to an improved final work. I also thank Kevin Burdge, Adolfo Carvalho, Jim Fuller, Ilkham Galiullin, Lynne Hillenbrand, Rocio Kiman, Dovi Poznanski, Tom Prince, Axel Schwope, the ZTF Variable Star Group, and the members of various groups to whom I have presented this tool during its inception. I thank Zach Vanderbosch for a well-written tool for downloading SDSS spectra. I thank the staffs of the Palomar and Keck Observatories for their assistance in carrying out observations. I am grateful for support from an NSF Graduate Fellowship.

I thank the LSSTC Data Science Fellowship Program, which is funded by LSSTC, NSF Cybertraining grant No. 1829740, the Brinson Foundation, and the Moore Foundation; my participation in the program has benefited this work.

Based on observations obtained with XMM-Newton, an ESA science mission with instruments and contributions directly funded by ESA Member States and NASA. This work has made use of data from the European Space Agency (ESA)

mission Gaia (https://www.cosmos.esa.int/gaia), processed by the Gaia Data Processing and Analysis Consortium (DPAC, https://www.cosmos.esa.int/web/gaia/dpac/consortium). Funding for the DPAC has been provided by national institutions, in particular the institutions participating in the Gaia Multilateral Agreement.

Based on observations obtained with the Samuel Oschin Telescope 48 inch and the 60 inch Telescope at the Palomar Observatory as part of the Zwicky Transient Facility project. ZTF is supported by the National Science Foundation under grant Nos. AST-1440341 and AST-2034437 and a collaboration including current partners Caltech, IPAC, the Weizmann Institute of Science, the Oskar Klein Center at Stockholm University, the University of Maryland, Deutsches Elektronen-Synchrotron and Humboldt University, the TANGO Consortium of Taiwan, the University of Wisconsin at Milwaukee, Trinity College Dublin, Lawrence Livermore National Laboratories, IN2P3, University of Warwick, Ruhr University Bochum, Northwestern University and former partners the University of Washington, Los Alamos National Laboratories, and Lawrence Berkeley National Laboratories. Operations are conducted by COO, IPAC, and UW.

Funding for the Sloan Digital Sky Survey V has been provided by the Alfred P. Sloan Foundation, the Heising-Simons Foundation, the National Science Foundation, and the Participating Institutions. SDSS acknowledges support and resources from the Center for High-Performance Computing at the University of Utah. SDSS telescopes are located at Apache Point Observatory, funded by the Astrophysical Research Consortium and operated by New Mexico State University, and at Las Campanas Observatory, operated by the Carnegie Institution for Science. The SDSS website is www.sdss.org.

SDSS is managed by the Astrophysical Research Consortium for the Participating Institutions of the SDSS Collaboration, including Caltech, The Carnegie Institution for Science, Chilean National Time Allocation Committee (CNTAC) ratified researchers, The Flatiron Institute, the Gotham Participation Group, Harvard University, Heidelberg University, The Johns Hopkins University, LEcole polytechnique fédérale de Lausanne (EPFL), Leibniz-Institut für Astrophysik Potsdam (AIP), Max-Planck-Institut für Astronomie (MPIA Heidelberg), Max-Planck-Institut für Extraterrestrische Physik (MPE), Nanjing University, National Astronomical Observatories of China (NAOC), New Mexico State University, The Ohio State University, Pennsylvania State University, Smithsonian Astrophysical Observatory, Space Telescope Science Institute (STScI), the Stellar Astrophysics Participation Group, Universidad Nacional Autónoma de México, University of Arizona, University of Colorado Boulder, University of Illinois at Urbana-Champaign, University of Toronto, University of Utah, University of Virginia, Yale University, and Yunnan University.

This work is based on data from eROSITA, the soft X-ray instrument aboard SRG, a joint Russian-German science mission supported by the Russian Space Agency (Roskosmos), in the interests of the Russian Academy of Sciences represented by its Space Research Institute (IKI), and the Deutsches Zentrum für Luft- und Raumfahrt (DLR). The SRG spacecraft was built by Lavochkin Association (NPOL) and its subcontractors, and is operated by NPOL with support from the Max Planck Institute for Extraterrestrial Physics (MPE). The development and construction of the eROSITA X-ray instrument was led by MPE, with contributions from the Dr. Karl Remeis Observatory Bamberg & ECAP (FAU Erlangen-Nuernberg), the University of Hamburg Observatory, the Leibniz Institute for Astrophysics Potsdam (AIP), and the Institute for Astronomy and Astrophysics of the University of Tübingen, with the support of DLR and the Max Planck Society. The Argelander Institute for Astronomy of the University of Bonn and the Ludwig Maximilians Universität Munich also participated in the science preparation for eROSITA.

Software: Python and the following libraries: matplotlib Hunter 2007, scipy Virtanen et al. 2020, astropy Astropy Collaboration et al. 2013, numpy van der Walt et al. 2011. PypeIt Prochaska et al. 2020, lpipe Perley 2019, and Tool for OPerations on Catalogues And Tables (TOPCAT) Taylor 2005.

Appendix A New Cataclysmic Variables from XMM-Newton: Description of Observations and Individual Systems

All systems are summarized in Table 1.

4XMM J001830.2+43571 (4XMMJ0018) was observed due to its 2.22 hr periodicity in ZTF. This system shows Balmer emission lines as well as prominent bumps centered at 4000 and 5000 Å. These are reminiscent of cyclotron harmonics in polars, leading me to classify it as a candidate polar (e.g., Warner 1995). The narrow emission lines, however, suggest this could be either a low-state polar or low accretion rate polar (e.g., Schwope et al. 2007).

4XMM J001912.5+220732 (4XMMJ0019) stood out due to its placement near the WD track in the Gaia HR diagram. This object shows nearly no variability in ZTF, making it unlikely to have been discovered had it not been for its X-ray detection. It features strong, double-peaked Balmer and He emission lines, with weak H β and H γ absoprtion from the WD, leading me to classify it as a candidate WZ Sge CV (e.g., Gilliland et al. 1986; Inight et al. 2023).

4XMM J021902.2+625713 (4XMMJ0219) stood out due to its placement near the main sequence despite having a 3.85 hr period in ZTF. The lack of strong Balmer emission lines (only weak H α is seen) as well as the FG-type spectrum is suggestive of the evolved CVs also known as pre-ELMs (El-Badry et al.

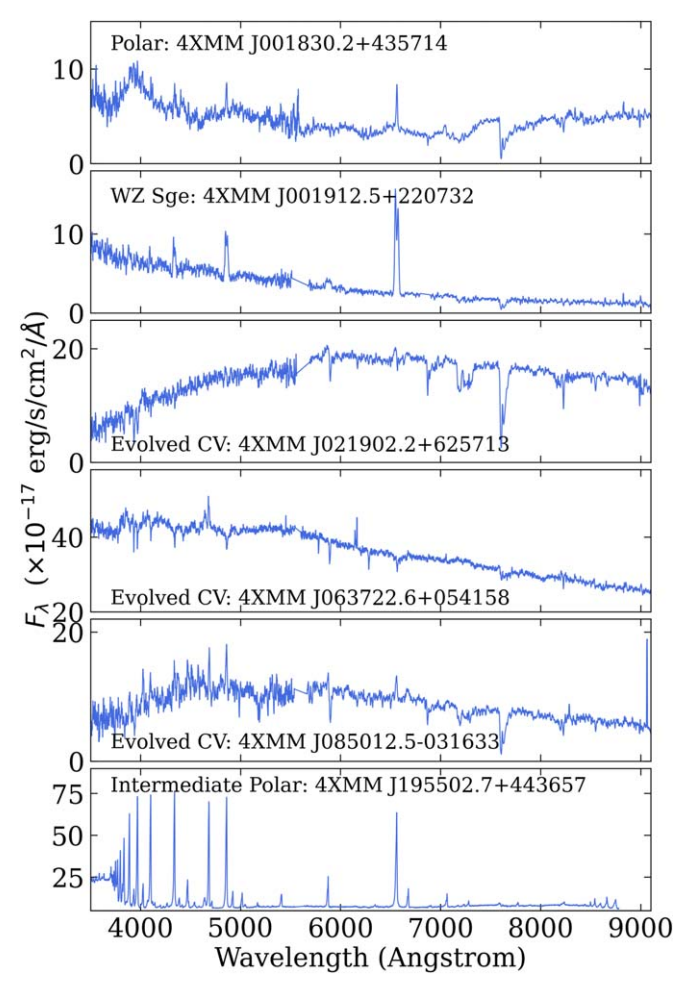


Figure 9. Keck and Palomar spectra of six CVs which are part of an ongoing spectroscopic survey of the 4XMM-Gaia catalog. All sources were predicted to be accreting compact objects using the X-ray Main Sequence, and confirmed through optical spectroscopy. Sub-classes shown are preliminary, yet all systems are distinct from archetypal CVs (dwarf novae such as that shown in Figure 5), demonstrating the richness that X-ray + optical surveys can reveal.

2021). In these systems, the WD accretes from a donor that filled its Roche lobe just before leaving the main sequence, therefore forming an "evolved" CV. Many systems evolve to short ($P_{\rm orb} < 1$ hr) periods before detaching and forming an extremely low mass (ELM) WD (El-Badry et al. 2021). Virtually all of the criteria are met for me to classify this system as an (pre-ELM) evolved CV.

4XMM J063722.6+054158 (4XMMJ0637) was selected due to its long orbital period ($P_{\rm orb}=13.8~\rm hr$) dominated by ellipsoidal modulation. It also undergoes regular, triangular-shaped outbursts, which last $\sim\!200~\rm days$, in contrast to typical dwarf nova outbursts which last $\sim\!10~\rm days$. At its orbital period, the donor must be an evolved subgiant (e.g., Sokolovsky et al. 2022). The optical spectrum is indeed dominated by the FG-type donor, albeit with He II 4686 and the rare CIII/NIII

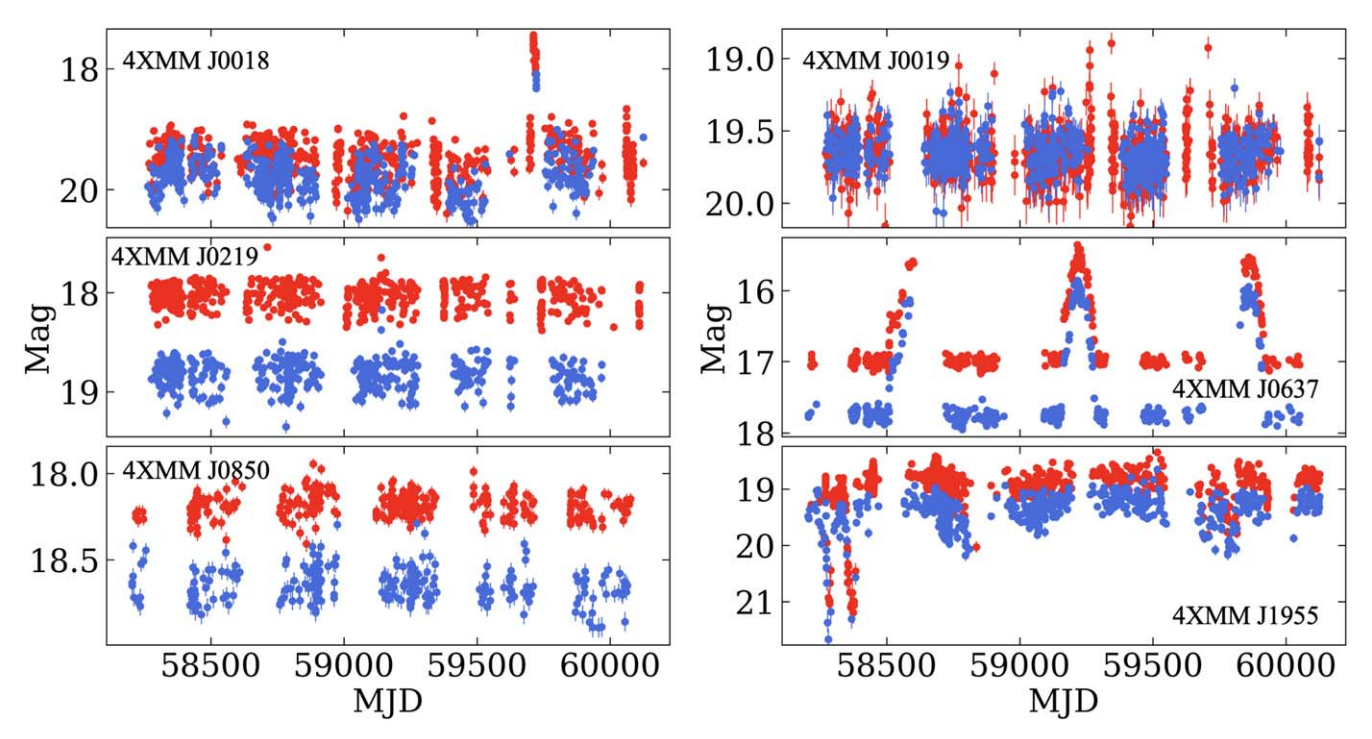


Figure 10. Long term (5 yr) ZTF light curves in r band (red) and g band (blue) of all newly discovered XMM CVs.

Bowen blend emission lines. Interestingly, this system is near the "bifurcation period," where depending on the WD and donor parameters, the system may either evolve to longer or shorter orbital periods (e.g., Belloni & Schreiber 2023). All of the criteria are met for me to classify this system as an evolved CV, and I will report on extensive spectroscopy in an upcoming study A. C. Rodriguez et al. (2024, in preparation).

4XMM J085012.5-03163 (4XMMJ0850) stood out due to its 51 minutes (or doubled, 1.70 hr) period in ZTF data. Phase-resolved spectroscopy is being acquired to determine the true period. Like 4XMMJ0219, this system is also unusually close to the main sequence for so short an orbital period (even if 1.70 hr is the true period). The spectrum is dominated by a K-type donor, which hints at it being an evolved CV. In this system, however, Balmer lines are in emission along with the He II 4686 line, which is not typically seen in pre-ELMs, but suggestive of magnetism (Silber 1992; El-Badry et al. 2021). While some characteristics lead me to classify this system as a candidate evolved CV, further work is needed to determine its true nature.

4XMM J195502.7+443657 (4XMMJ1955) features unusual variability in ZTF—low amplitude (<1 mag) variability with high amplitude (~3 mag), short (~20 days) dips. High-cadence ZTF data also reveals a 20–30 minutes period, suggestive of a WD spin period in intermediate polars (Mukai 2017). Remarkably, its optical spectrum shows the strongest Balmer and He emission lines of any object in the sample. He II 4686 is also

nearly as strong as $H\beta$, which is typically seen in intermediate polars (Silber 1992). Despite fulfilling some of the necessary criteria, I am cautious to label this system as a candidate intermediate polar since extensive X-ray and optical timing data as well as phase-resolved spectroscopy are usually needed to securely classify such systems.

Of the six systems reported above, four were observed with the Double Spectrograph (DBSP; Oke & Gunn 1982) on the Hale telescope (4XMMJ0018, 4XMMJ0019 4XMMJ0219, and 4XMMJ0850). I used the 600/4000 grism on the blue side and the 316/7500 grating on the red side. A 1."5 slit was used, and the seeing throughout all observations varied between 1."5 and 2."0, leading to some slit losses. All P200/DBSP data were reduced with DBSP-DRP, 10 a Python-based pipeline optimized for DBSP built on the more general PypeIt pipeline (Prochaska et al. 2020).

4XMMJ0637 and 4XMMJ1955 were observed with the Keck I telescope using the Low-Resolution Imaging Spectrometer (LRIS; Oke et al. 1995). I used the 600/4000 grism on the blue side with 2×2 binning (spatial, spectral), and the 600/7500 grating on the red side with 2×1 binning. I used a 1.0 slit, and the seeing each night was approximately 0.7-1, leading to minimal slit losses. All Keck I/LRIS data were reduced with lpipe, an IDL-based pipeline optimized for LRIS long slit spectroscopy and imaging (Perley 2019). All data (for both

¹⁰ https://dbsp-drp.readthedocs.io/en/stable/index.html

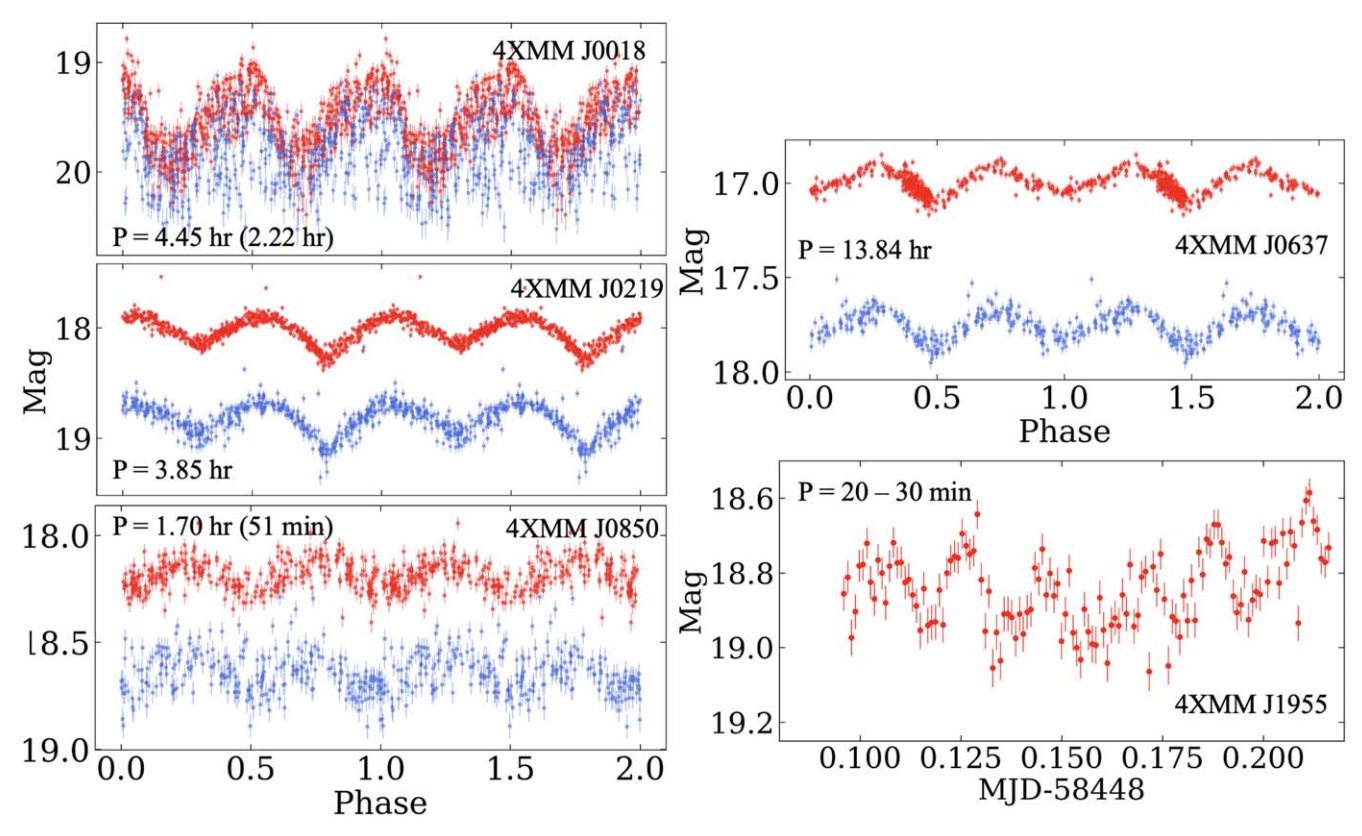


Figure 11. Folded ZTF light curves (excluding outbursts) in *r* band (red) and *g* band (blue) of 4 newly discovered XMM CVs. On the bottom right are the high-cadence continuous observations of 4XMMJ1955 from the ZTF Galactic Plane Survey.

 $\begin{tabular}{ll} \textbf{Table 1} \\ \textbf{Summary of all Newly Discovered XMM CVs} \\ \end{tabular}$

Name	Gaia R.A. (deg)	Gaia Decl. (deg)	Classification	Orbital Period (hr)
4XMM J001830.2+435714	4.626476	43.954572	CV (Polar)	2.22 (4.45)
4XMM J001912.5+220732	4.802370	22.125808	CV (WZ Sge)	•••
4XMM J021902.2+625713	34.760214	62.953643	CV (evolved)	3.85
4XMM J063722.6+054158	99.344615	5.699567	CV (evolved)	13.8
4XMM J085012.5-031633	132.552197	-3.276101	CV (evolved)	1.70 (0.85)
4XMM J195502.7+443657	298.761724	44.616101	CV (Intermediate Polar)	

Note. The most likely orbital period is listed first, and the one in parentheses cannot be ruled out without additional data.

DBSP and LRIS) were flat fielded sky-subtracted using standard techniques. Internal arc lamps were used for the wavelength calibration and a standard star for overall flux calibration.

In Figure 10, I present long term ZTF light curves for all CVs in Section 4.3, from Data Release 19 (covering 2018 March–2023 July). ZTF is a photometric survey that uses a wide 47 \deg^2 field-of-view camera mounted on the Samuel Oschin 48 inch telescope at Palomar Observatory with g, r, and i filters (Bellm et al. 2019b; Graham et al. 2019; Masci et al. 2019; Dekany et al. 2020). In its first year of operations, ZTF

carried out a public nightly Galactic Plane Survey in *g*-band and *r*-band (Bellm et al. 2019a; Kupfer et al. 2021). This survey was in addition to the Northern Sky Survey which operated on a 3 day cadence (Bellm et al. 2019b). Since entering Phase II, the public Northern Sky Survey is now at a 2 days cadence. The pixel size of the ZTF camera is 1" and the median delivered image quality is 2."0 at FWHM.

In Figure 11, I present phase-folded light curves for four objects: 4XMMJ0018, 4XMMJ0219, 4XMMJ0850, and 4XMMJ0637. I used the gatspy software (Vanderplas 2015)

to compute a Lomb-Scargle periodogram (Scargle 1982), searching for periods between 4 minutes and 10 days with an oversampling factor of 5. For all four systems that show a significant (10σ above the median) periodicity, I plot twice the best period, which in 4XMMJ0219 and 4XMMJ0637 reveals ellipsoidal modulations (minima of different depths). However, in the case of 4XMMJ0018 and 4XMMJ0850, the difference between two different minima is unclear and phase-resolved spectroscopy is needed to reveal the true period. Finally, I present the high-cadence data from the ZTF Galactic Plane

Survey for 4XMMJ1955, which reveals pulsations on a 20–30 minutes timescale.

Appendix B Catalog Data

In Table 2, I list all of the objects used from external catalogs and references to the papers in which X-ray fluxes were reported. In Table 3, I show a preview of the entire XMM-Gaia crossmatched catalog, which I make available in machine readable format.

 Table 2

 All Systems Shown in Figure 1 with Literature X-Ray Detections

Name	Class	Gaia DR3 ID	X-ray Reference
J0212+5320	Redback	455282205716288384	(1)
J1048+2339	Redback	3990037124929068032	(1)
J1306-40	Redback	6140785016794586752	(1)
J1431-4715	Redback	6098156298150016768	(1)
J1622-0315	Redback	4358428942492430336	(1)
J1628-3205	Redback	6025344817107454464	(1)
J1723-2837	Redback	4059795674516044800	(1)
J1803-6707	Redback	6436867623955512064	(1)
J1816+4510	Redback	2115337192179377792	(1)
J1908+2105	Redback	4519819661567533696	(1)
J1910-5320	Redback	6644467032871428992	(1)
J2039-5618	Redback	6469722508861870080	(1)
J2129-0429	Redback	2672030065446134656	(1)
J2215+5135	Redback	2001168543319218048	(1)
J2339-0533	Redback	2440660623886405504	(1)
J1311-3430	Black Widow	6179115508262195200	(1)
J1653-0158	Black Widow	4379227476242700928	(1)
J1810+1744	Black Widow	4526229058440076288	(1)
B1957+20	Black Widow	1823773960079216896	(1)
GROJ0422+32	LMXB (BH)	172650748928103552	(2)
A0620-00	LMXB (BH)	3118721026600835328	(2)
V404 Cyg	LMXB (BH)	2056188624872569088	(2)
XTE J1118+480	LMXB (BH)	789430249033567744	(2)
GROJ1655-40	LMXB (BH)	5969790961312131456	(2)
4U 2129+47	LMXB (NS)	1978241050130301312	(3)
Cen X-4	LMXB (NS)	6205715168442046592	(3)
Aql X-1	LMXB (NS)	4264296556603631872	(3)
SAX J1808.4-3658	LMXB (NS)	4037867740522984832	(3)
A0535+26	HMXB (NS)	3441207615229815040	(4)
KS 1947+300	HMXB (NS)	2031939548802102656	(4)
V4641 Sgr	HMXB (BH)	4053096388919082368	(4)
Cyg X-1	HMXB (BH)	2059383668236814720	(4)
GX 1+4	Symbiotic (NS)	4110236324513030656	(5)
4U 1954+319	Symbiotic (NS)	2034031438383765760	(5)
CXOGBS J173620.2293338	Symbiotic (NS)	4060066227422719872	(5)
4U 1700+24	Symbiotic (NS)	4571810378118789760	(5)
NQ Gem	Symbiotic (WD)	868424696282795392	(6)
UV Aur	Symbiotic (WD)	180919213811383680	(6)
ZZ CMi	Symbiotic (WD)	3155368612444708096	(6)
ER Del	Symbiotic (WD)	1750795043999682304	` '
	•		(6)
CD -283719	Symbiotic (WD)	5608089951177429120	(6)
RX J0019.8+2156	SSS	2800287654443977344	(7)
RX J0925.7-4758	SSS	5422337322910734080	(7)
RR Tel	SSS	6448785024330499456	(7)

Reference. (1): Koljonen & Linares (2023), (2): Garcia et al. (2001), (3): Menou et al. (1999), (4): Russell et al. (2006), (5): Yungelson et al. (2019), (6): Luna et al. (2013), (7): 4XMM-DR13 Catalog.

 Table 3

 I Make the Full XMM-Gaia Crossmatch Freely Available in Machine Readable Format

4XMM-DR13 ID	IAUNAME	Gaia DR3 ID	Non-magnetic CV	YSO	Active Binary
201253101010037	4XMM J000009.8-251920	2335010480014243328	False	False	False
204033901010033	4XMM J000012.9+622946	429950007577101952	False	False	False
207009901010018	4XMM J000014.6+675337	528609770043800832	False	False	False
206584004010005	4XMM J000024.9+443634	385045506010558336	False	False	False
207009901010019	4XMM J000030.3+681159	528996042222710016	False	False	False
207009901010001	4XMM J000032.0+681500	528996591978497408	False	False	False
206935404010007	4XMM J000047.9+233216	2848395067729986688	False	False	False
206584004010038	4XMM J000102.0+442809	385041279762788608	False	False	False
206584004010048	4XMM J000110.9+443700	385043405769547136	False	False	False
204033901010077	4XMM J000129.2+622456	429945643890463488	False	False	False
200161401010017	4XMM J000130.0+625236	430053396031738112	False	False	False
206584004010017	4XMM J000139.7+442610	385028910256998528	False	False	True
206935404010018	4XMM J000146.9+233512	2848232133851323264	False	False	False
200417501010032	4XMM J000153.4-300612	2320841520343862400	False	False	False
204033901010016	4XMM J000153.6+623220	429947499316231808	False	False	False
200417501010078	4XMM J000154.4-301038	2320834614036455424	False	False	False
200417501010007	4XMM J000154.4-300741	2320835576109126400	False	False	False
204033901010056	4XMM J000155.6+622800	429946812121535488	False	False	False
200417501010112	4XMM J000157.0-301209	2320834304798813568	False	False	False
200417501010138	4XMM J000157.6-300929	2320834751475799808	False	False	False
•••					

Note. The first twenty rows, and select columns are shown here as a preview. (This table is available in its entirety in FITS format.)

ORCID iDs

Antonio C. Rodriguez https://orcid.org/0000-0003-4189-9668

```
References
Agüeros, M. A., Anderson, S. F., Covey, K. R., et al. 2009, ApJS, 181, 444
Akras, S., Guzman-Ramirez, L., Leal-Ferreira, M. L., & Ramos-Larios, G.
   2019, ApJS, 240, 21
Almeida, A., Anderson, S. F., Argudo-Fernández, M., et al. 2023, ApJS,
   267, 44
Amaro-Seoane, P., Audley, H., Babak, S., et al. 2017, arXiv:1702.00786
Armas Padilla, M., Corral-Santana, J. M., Borghese, A., et al. 2023, A&A,
   677, A186
Astropy Collaboration, Robitaille, T. P., Tollerud, E. J., et al. 2013, A&A,
   558, A33
Audard, M., Güdel, M., Sres, A., Raassen, A. J. J., & Mewe, R. 2003, A&A,
Bellm, E. C., Kulkarni, S. R., Barlow, T., et al. 2019a, PASP, 131, 068003
Bellm, E. C., Kulkarni, S. R., Graham, M. J., et al. 2019b, PASP, 131, 018002
Belloni, D., & Schreiber, M. R. 2023, in Handbook of X-ray and Gamma-ray
   Astrophysics, ed. C. Bambi & A. Santangelo (Singapore: Springer), 129
Boller, T., Freyberg, M. J., Trümper, J., et al. 2016, A&A, 588, A103
Bolton, C. T. 1972, Natur, 235, 271
Bopp, B. W., & Stencel, R. E. 1981, ApJL, 247, L131
Bouvier, J., Bertout, C., Benz, W., & Mayor, M. 1986, A&A, 165, 110
Bowyer, S., Byram, E. T., Chubb, T. A., & Friedman, H. 1965, Sci, 147, 394
Braes, L. L. E., & Miley, G. K. 1971, Natur, 232, 246
Brunner, H., Liu, T., Lamer, G., et al. 2022, A&A, 661, A1
Charbonneau, P. 2014, ARA&A, 52, 251
Choi, J., Dotter, A., Conroy, C., et al. 2016, ApJ, 823, 102
Dalton, G., Trager, S. C., Abrams, D. C., et al. 2012, Proc. SPIE, 8446, 84460P
de Jong, R. S., Agertz, O., Berbel, A. A., et al. 2019, Msngr, 175, 3
Dekany, R., Smith, R. M., Riddle, R., et al. 2020, PASP, 132, 038001
```

```
DESI Collaboration, Aghamousa, A., Aguilar, J., et al. 2016, arXiv:1611.
El-Badry, K., Rix, H.-W., Quataert, E., Kupfer, T., & Shen, K. J. 2021,
           5, 508, 4106
Evans, I. N., & Civano, F. 2018, A&G, 59, 2.17
Evans, P. A., Page, K. L., Osborne, J. P., et al. 2020, ApJS, 247, 54
Feigelson, E. D., Broos, P., Gaffney, J. A. I., et al. 2002, ApJ, 574, 258
Feigelson, E. D., & Kriss, G. A. 1981, ApJL, 248, L35
Freund, S., Czesla, S., Robrade, J., Schneider, P. C., & Schmitt, J. H. M. M.
  2022, A&A, 664, A105
Gaia Collaboration, Brown, A. G. A., Vallenari, A., et al. 2021, A&A, 649, A1
Gaia Collaboration, Prusti, T., de Bruijne, J. H. J., et al. 2016, A&A, 595, A1
Gaia Collaboration, Vallenari, A., Brown, A. G. A., et al. 2023, A&A, 674, A1
Garcia, M. R., McClintock, J. E., Narayan, R., et al. 2001, ApJL, 553, L47
Giacconi, R., Branduardi, G., Briel, U., et al. 1979, ApJ, 230, 540
Gilliland, R. L., Kemper, E., & Suntzeff, N. 1986, ApJ, 301, 252
Graham, M. J., Kulkarni, S. R., Bellm, E. C., et al. 2019, PASP, 131, 078001
Green, G. M., Schlafly, E., Zucker, C., Speagle, J. S., & Finkbeiner, D. 2019,
   ApJ, 887, 93
Greiner, J., & Richter, G. A. 2015, A&A, 575, A42
Guidry, J. A., Vanderbosch, Z. P., Hermes, J. J., et al. 2021, ApJ, 912, 125
Güver, T., & Özel, F. 2009, MNRAS, 400, 2050
Hailey, C. J., Mori, K., Perez, K., et al. 2016, ApJ, 826, 160
Hartmann, L., Herczeg, G., & Calvet, N. 2016, ARA&A, 54, 135
Hunter, J. D. 2007, CSE, 9, 90
Inight, K., Gänsicke, B. T., Breedt, E., et al. 2023, MNRAS, 524, 4867
Jackim, R., Szkody, P., Hazelton, B., & Benson, N. C. 2020, RNAAS, 4, 219
Johnstone, C. P., Bartel, M., & Güdel, M. 2021, A&A, 649, A96
Kahabka, P., & van den Heuvel, E. P. J. 1997, ARA&A, 35, 69
Ivezić, Ž., Kahn, S. M., Tyson, J. A., et al. 2019, ApJ, 873, 111
Kochanek, C. S., Shappee, B. J., Stanek, K. Z., et al. 2017, PASP, 129, 104502
Koljonen, K. I. I., & Linares, M. 2023, MNRAS, 525, 3963
Kollmeier, J. A., Zasowski, G., Rix, H.-W., et al. 2017, arXiv:1711.03234
Kupfer, T., Prince, T. A., van Roestel, J., et al. 2021, MNRAS, 505, 1254
Lewin, W. H. G., van Paradijs, J., & Taam, R. E. 1993, SSRv, 62, 223
Lin, D., Webb, N. A., & Barret, D. 2012, ApJ, 756, 27
```

```
Lo, K. K., Farrell, S., Murphy, T., & Gaensler, B. M. 2014, ApJ, 786, 20
Luna, G. J. M., Sokoloski, J. L., Mukai, K., & Nelson, T. 2013, A&A, 559, A6
Maccacaro, T., Gioia, I. M., Wolter, A., Zamorani, G., & Stocke, J. T. 1988,
   ApJ, 326, 680
Magaudda, E., Stelzer, B., Covey, K. R., et al. 2020, A&A, 638, A20
Marton, G., Ábrahám, P., Szegedi-Elek, E., et al. 2019, MNRAS, 487, 2522
Masci, F. J., Laher, R. R., Rusholme, B., et al. 2019, PASP, 131, 018003
Menou, K., Esin, A. A., Narayan, R., et al. 1999, ApJ, 520, 276
Mowlavi, N., Rimoldini, L., Evans, D. W., et al. 2021, A&A, 648, A44
Mukai, K. 2017, PASP, 129, 062001
Murdin, P., & Webster, B. L. 1971, Natur, 233, 110
Nelemans, G., Yungelson, L. R., & Portegies Zwart, S. F. 2001, A&A,
Núñez, A., Agüeros, M. A., Curtis, J. L., et al. 2023, ApJ, 962, 12
Oke, J. B., Cohen, J. G., Carr, M., et al. 1995, PASP, 107, 375
Oke, J. B., & Gunn, J. E. 1982, PASP, 94, 586
Pallavicini, R., Golub, L., Rosner, R., et al. 1981, ApJ, 248, 279
Perley, D. A. 2019, PASP, 131, 084503
Predehl, P., Andritschke, R., Arefiev, V., et al. 2021, A&A, 647, A1
Prochaska, J., Hennawi, J., Westfall, K., et al. 2020, JOSS, 5, 2308
Reiners, A., Schüssler, M., & Passegger, V. M. 2014, ApJ, 794, 144
Reiners, A., Shulyak, D., Käpylä, P. J., et al. 2022, A&A, 662, A41
Revnivtsev, M., Sazonov, S., Gilfanov, M., Churazov, E., & Sunyaev, R. 2006,
    A&A, 452, 169
Ricker, G. R., Winn, J. N., Vanderspek, R., et al. 2015, JATIS, 1, 014003
Ritter, H., & Kolb, U. 2003, A&A, 404, 301
Rodriguez, A. C., Galiullin, I., Gilfanov, M., et al. 2023a, ApJ, 954, 63
Rodriguez, A. C., Kulkarni, S. R., Prince, T. A., et al. 2023b, ApJ, 945, 141
Romani, R. W., & Sanchez, N. 2016, ApJ, 828, 7
Russell, D. M., Fender, R. P., Hynes, R. I., et al. 2006, MNRAS, 371, 1334
Salvato, M., Buchner, J., Budavári, T., et al. 2018, MNRAS, 473, 4937
Salvato, M., Wolf, J., Dwelly, T., et al. 2022, A&A, 661, A3
Sasaki, R., Tsuboi, Y., Iwakiri, W., et al. 2021, ApJ, 910, 25
Scargle, J. D. 1982, ApJ, 263, 835
Schmitt, J. H. M. M., Fleming, T. A., & Giampapa, M. S. 1995, ApJ, 450, 392
Schwope, A., Buckley, D. A. H., Kawka, A., et al. 2022, A&A, 661, A42
Schwope, A., Kurpas, J., Baecke, P., et al. 2024, arXiv:2401.17304
```

```
Schwope, A. D., Staude, A., Koester, D., & Vogel, J. 2007, A&A, 469, 1027
Silber, A. D. 1992, PhD thesis, Massachusetts Institute of Technology
Skumanich, A. 1972, ApJ, 171, 565
Sokolovsky, K. V., Strader, J., Swihart, S. J., et al. 2022, ApJ, 934, 142
Stelzer, B., Klutsch, A., Coffaro, M., Magaudda, E., & Salvato, M. 2022,
Stelzer, B., Marino, A., Micela, G., López-Santiago, J., & Liefke, C. 2013,
  MNRAS, 431, 2063
Stocke, J. T., Morris, S. L., Gioia, I. M., et al. 1991, ApJS, 76, 813
Sunyaev, R., Arefiev, V., Babyshkin, V., et al. 2021, A&A, 656, A132
Tauris, T. M., & van den Heuvel, E. P. J. 2023, Physics of Binary Star
  Evolution. From Stars to X-ray Binaries and Gravitational Wave Sources
  (Princeton, NJ: Princeton Univ. Press)
Taylor, M. B. 2005, in ASP Conf. Ser. 347, Astronomical Data Analysis
  Software and Systems XIV, ed. P. Shopbell, M. Britton, & R. Ebert (San
  Francisco: ASP), 29
Tonry, J. L., Denneau, L., Heinze, A. N., et al. 2018, PASP, 130, 064505
Tranin, H., Godet, O., Webb, N., & Primorac, D. 2022, A&A, 657, A138
Truemper, J. 1982, AdSpR, 2, 241
van der Walt, S., Colbert, S. C., & Varoquaux, G. 2011, CSE, 13, 22
van Paradijs, J., Penninx, W., & Lewin, W. H. G. 1988, MNRAS, 233, 437
Vanderplas, J. 2015, gatspy: General Tools for Astronomical Time Series in
  Python, v0.1.1, Zenodo, doi:10.5281/zenodo.14833
Virtanen, P., Gommers, R., Oliphant, T. E., et al. 2020, NatMe, 17, 261
Voges, W., Aschenbach, B., Boller, T., et al. 1999, A&A, 349, 389
Vogt, S. S., Soderblom, D. R., & Penrod, G. D. 1983, ApJ, 269, 250
Walter, F. M., & Bowyer, S. 1981, ApJ, 245, 671
Warner, B. 1995, Cataclysmic Variable Stars, Vol. 28 (Cambridge: Cambridge
  Univ. Press)
Webb, N. A., Coriat, M., Traulsen, I., et al. 2020, A&A, 641, A136
Webster, B. L., & Murdin, P. 1972, Natur, 235, 37
Worrall, D. M., & Marshall, F. E. 1983, ApJ, 267, 691
Wright, N. J., Drake, J. J., Mamajek, E. E., & Henry, G. W. 2011, ApJ, 743,
York, D. G., Adelman, J., Anderson, J. E. J., et al. 2000, AJ, 120, 1579
Yungelson, L. R., Kuranov, A. G., & Postnov, K. A. 2019, MNRAS, 485, 851
```

Schwope, A., Marsh, T. R., Standke, A., et al. 2023, A&A, 674, L9